Chinese Chemical Letters 34 (2023) 107788

Contents lists available at ScienceDirect

Chinese Chemical Letters

journal homepage: www.elsevier.com/locate/cclet

Heterointerface engineering of Ru/RuS_2 on N/S-doped hollow mesoporous carbon for promoting alkaline hydrogen evolution

Ning Wang[a], Dong-Dong Ma[a], Sheng-Hua Zhou[a], Meng-Ke Hu[a], Xiaofang Li[a,*], Xin-Tao Wu[a,d], Qi-Long Zhu[a,b,c,d,*]

[a] *State Key Laboratory of Structural Chemistry, Fujian Institute of Research on the Structure of Matter, Chinese Academy of Sciences (CAS), Fuzhou 350002, China*
[b] *Fujian Science & Technology Innovation Laboratory for Optoelectronic Information of China, Fuzhou 350108, China*
[c] *College of Chemistry and Chemical Engineering, Jiangxi Normal University, Nanchang 330022, China*
[d] *University of Chinese Academy of Sciences, Beijing 100049, China*

ARTICLE INFO

Article history:
Received 16 June 2022
Revised 22 July 2022
Accepted 24 August 2022
Available online 28 August 2022

Keywords:
Hydrogen evolution reaction
Heterostructures
N/S-doped carbon
Hollow mesoporous microspheres
Ru nanoparticles

ABSTRACT

Alkaline hydrogen evolution reaction (HER) suffers from a sluggish kinetic, which requires the elaborate catalytic interface and micro-nanoscale architecture engineering of the electrocatalysts to accelerate the water dissociation and hydrogen evolution. Herein, the heterointerface engineering was proposed for promoting the alkaline HER by constructing the highly exposed Ru/RuS_2 heterostructures homogeneously distributed on hollow N/S-doped carbon microspheres (Ru/RuS_2@h-NSC). Benefited from the synergistic effect of heterointerfacial Ru/RuS_2, the high accessibility of the active sites on both inner and outer surface of mesoporous shells and the efficient mass transport, Ru/RuS_2@h-NSC affords a remarkable catalytic performance with an overpotential of 26 mV@10 mA/cm^2 for alkaline HER, outperforming most of the state-of-the-art catalysts. Further applying Ru/RuS_2@h-NSC and its oxidized derivate for the overall alkaline water splitting, the required cell voltage is much lower than that of the commercial Pt/C||RuO_2 pair to achieve the same current density. Our study may allow us to guide the design of micro-nanoreactors with optimal catalytic interfaces for promising electrocatalytic applications.

The severe energy and environmental crises urgently call for the development of sustainable energy. Hydrogen as one of the most promising alternatives can be sustainably produced by water splitting powered by renewable energy source [1–3]. Hydrogen evolution reaction (HER) can be realized in acidic, basic and neutral media, among which the alkaline/neutral HER suffers from the sluggish kinetic due to requiring an additional water dissociation step, leading to the higher overpotential and energy cost [4–8]. Platinum (Pt) is recognized as the most active metal for HER, while the high expense and scarce reservoir greatly limit its commercial application. As an alternative, ruthenium (Ru) is of economic advantage with about a quarter price of Pt. More importantly, the unique electronic structure endows Ru with a lower energy barrier for water dissociation and a relatively strong bonding strength with hydrogen, which makes the Ru-based electrocatalysts applicable for alkaline HER [9–12]. The past years have witnessed great advance in developing efficient Ru-based electrocatalysts for alkaline HER; however, it is still challenging to achieve the low overpotentials analogous to those of the Pt-based catalysts in acidic condition.

Various approaches have been employed to optimize the catalytic activity of Ru-based electrocatalysts, such as alloying with the secondary metals [13–17], isolating single atoms on porous carbons [18–20] and constructing specific nanostructures [10,21–23]. Among various nanostructures, the catalysts with heterostructures may play synergistic effect by the interface engineering, which is able to precisely modulate the catalytic activity [24–26]. For one thing, the electronic structures of active sites can be effectively manipulated to favor the activation of the substrates and the absorption of various intermediates [26,27]. For another, the stepwise reactions may require different active species, during which the well-defined heterostructure can enable diverse reactions to go smoothly over different active sites, thus accelerating the reaction kinetics [28,29]. Up to now, several kinds of Ru-based heterostructures, mainly metal/metal oxides, have been reported for efficient alkaline HER, such as Ru-MoO_2 [22], Ru-RuO_2/CNT [30]. Generally, the heterostructures can be obtained by pyrolyzing corresponding precursors; however, the random distribution of these sources dur-

---

* Corresponding authors at: State Key Laboratory of Structural Chemistry, Fujian Institute of Research on the Structure of Matter, Chinese Academy of Sciences (CAS), Fuzhou 350002, China.
E-mail addresses: lixiaofang@fjirsm.ac.cn (X. Li), qlzhu@fjirsm.ac.cn (Q.-L. Zhu).

https://doi.org/10.1016/j.cclet.2022.107788

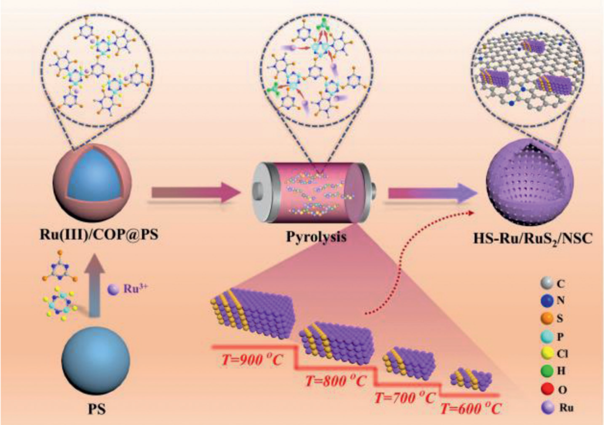

Fig. 1. Schematic illustration for the preparation of Ru/RuS_2@h-NSC.

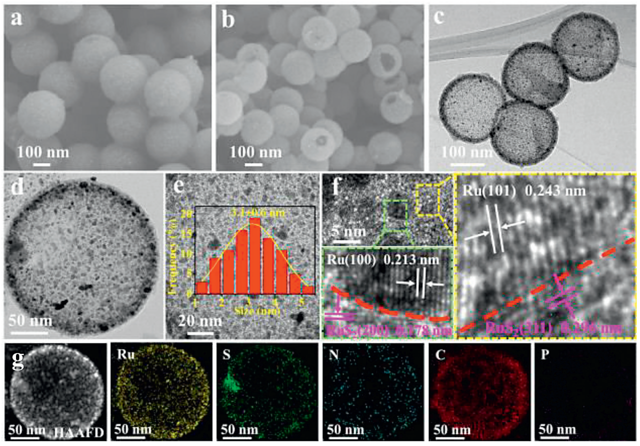

Fig. 2. SEM images of (a) Ru(III)/COP@PS and (b) Ru/RuS_2@h-NSC. (c, d) TEM images of Ru/RuS_2@h-NSC. (e) TEM image of distributed Ru/RuS_2 NPs (inset: corresponding size distribution). (f) HRTEM image of the Ru/RuS_2 heterointerface. (g) HAADF-STEM and corresponding mapping images of Ru, S, N, C and P elements over Ru/RuS_2@h-NSC.

ing the thermal treatment restrains the formation of the distinct interfaces. Developing a controllable strategy for acquiring the homogeneously distributed heterostructures is highly desirable.

Covalent organic polymers (COPs) are constructed with lightweight elements by covalent bonds and have been widely developed owning to their tunable structures with desired multi-element compositions and high surface areas [31–34]. With these merits of COPs, the heterointerface engineering was proposed for promoting the alkaline HER by constructing the Ru/RuS_2 heterostructures homogeneously distributed on hollow N/S-doped carbon microspheres (Ru/RuS_2@h-NSC), with the P/S/N-rich COP encapsulated polystyrene spheres (COP@PS) as the template. The decomposition of the P/S/N-rich COP@PS during pyrolysis can release bountiful P/S/N-containing gas, during which the P-abundant COP is conducive to the trap of Ru(III) species and facilitates the formation of the highly exposed Ru/RuS_2 heterostructures. Benefited from the synergistic effect of heterointerfacial Ru/RuS_2, the high accessibility of the active sites on the mesoporous shells and the efficient mass transport, the as-prepared Ru/RuS_2@h-NSC exhibits a phenomenal electrocatalytic performance with an overpotential of 26 mV@10 mA/cm^2 and a Tafel slope of 73.6 mV/dec for alkaline HER, outperforming most of the state-of-the-art catalysts. Furthermore, by assembling the electrolyzer with Ru/RuS_2@h-NSC and derived hollow RuO_2 nanobowls (h-RuO_2) as the cathodic and anodic catalysts, respectively, for overall water splitting, the required cell voltage of Ru/RuS_2@h-NSC||h-RuO_2 is 100 mV lower than that of the commercial Pt/C||RuO_2 cell to achieve the current density of 10 mA/cm^2. Our study may allow us to guide the design of micro-nanoreactors with optimal catalytic interfaces for various promising electrocatalytic applications.

The schematic illustration for the preparation of Ru/RuS_2@h-NSC is shown in Fig. 1. Firstly, PS microspheres were used as the template to guide the uniform growth of COP *via* the *in-situ* polymerization of trithiocyanuric acid (TCA) and phosphonitrilic chloride trimer (PCT), resulting in the core-shell COP@PS composite. The IR spectrum of COP@PS in Fig. S1 (Supporting information) shows the characteristic peaks of C=N, P=N, C=S and P−N bonds, testifying the successful polymerization [35–37]. Benefited from the abundant P, N, S sites of COP with unsaturated coordination, Ru(III) ions were easily adsorbed to obtain the Ru(III)/COP@PS composite, as verified by the apparent color change from white to brown upon the Ru(III) adsorption (Fig. S2 in Supporting information). The spherical structure with rough surface of Ru(III)/COP@PS can be detected by scanning electron microscopy (SEM) (Fig. 2a and Fig. S3 in Supporting information), further indicating the successful coating of Ru(III)/COP around the PS templates. The powder X-ray diffraction (PXRD) pattern in Fig. S4 (Supporting information) shows that Ru(III)/COP@PS is amorphous. Then, the obtained Ru(III)/COP@PS was further pyrolyzed in Ar atmosphere, during which the inner PS cores were consumed while the outer P/S/N-rich COP was decomposed to release bountiful P/S/N-containing gas, leading to the hollow N/S-doped carbon microspheres immobilized with the Ru/RuS_2 heterostructures, labelled as Ru/RuS_2@h-NSC. To explore the structural evolution of Ru/RuS_2@h-NSC under pyrolysis, the PXRD patterns of the samples obtained at different calcination temperatures were shown in Fig. S5 (Supporting information), which exhibit two sets of distinct diffraction peaks at 38.4°/44.0°/58.3° and 27.5°/31.9°/54.2° corresponding to the hexagonal Ru and RuS_2 phases, respectively, suggesting the symbiotic formation of both Ru and RuS_2 phases. Furthermore, the derived samples well inherited the maternal spherical shell structure of Ru(III)/COP@PS at a pyrolysis temperature up to 800 °C and the hollow cavity can be clearly observed in the broken spheres (Fig. S6 in Supporting information). While increasing the pyrolysis temperature to 900 °C can lead to the obvious collapse of the hollow microsphere. In addition, to probe the role of PS in guiding the microspherical morphology, Ru(III)/COP was directly pyrolyzed at 800 °C. As shown in Fig. S7 (Supporting information), only aggregated RuS_2 particles on carbon (RuS_2@NSC) were obtained without PS, which indicates that the PS can not only act as the template of the hollow microspherical structure, but also provide a reductive atmosphere to form the Ru NPs in the Ru/RuS_2 heterostructures [38].

The transmission electron microscopy (TEM) image in Fig. 2c further verifies the hollow spherical structure of Ru/RuS_2@h-NSC, in agreement with the observation in SEM image (Fig. 2b), which was well inherited from the maternal spherical structure of Ru(III)/COP@PS. The shell thickness of the hollow spherical structure is about 15 nm, and the homogeneously distributed Ru/RuS_2 NPs with an average size of about 3.1 nm can be observed on the shell (Figs. 2c–e). In the high-resolution TEM (HRTEM) image in Fig. 2f, the heterointerfaces between the lattice fringes of Ru and RuS_2 are clearly distinguishable (highlighted in boxes), of which the obvious lattice fringes with the spacings of 0.243 and 0.213 nm can be ascribed to the (101) and (100) planes of the hexagonal Ru phase, while the adjacent lattice fringes with the spacings of 0.296 and 0.178 nm are attributed to the (311) and (200) planes of RuS_2. The HAADF-STEM and the corresponding elemental mapping of Ru/RuS_2@h-NSC are shown in Fig. 2g and Fig. S8 (Supporting information). Combined with the energy-dispersive X-ray (EDX)

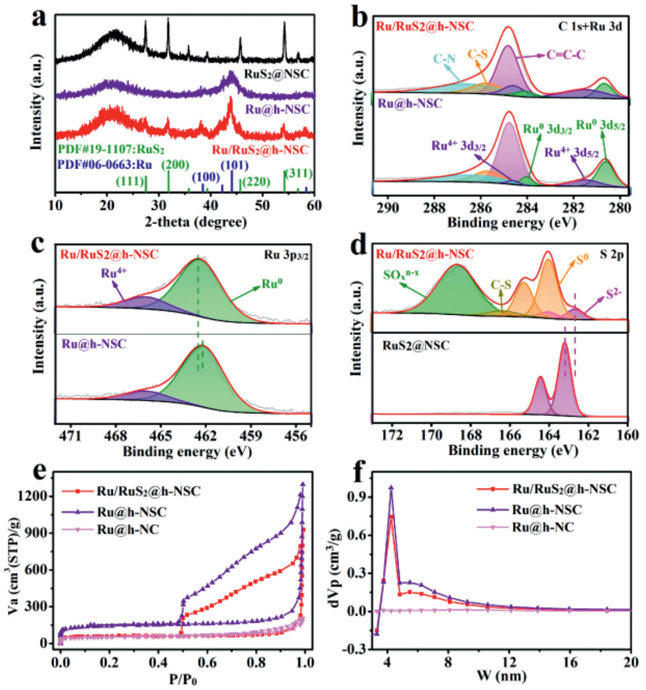

Fig. 3. (a) PXRD spectra of Ru/RuS_2@h-NSC, Ru@h-NSC and RuS_2@NSC. (b, c) High-resolution C 1s + Ru 3d spectra and Ru 3p spectra of Ru/RuS_2@h-NSC and Ru@h-NSC. (d) High-resolution S 2p spectra of Ru/RuS_2@h-NSC and RuS_2@NSC. (e) N_2 sorption isotherms and (f) corresponding pore size distribution of Ru/RuS_2@h-NSC, Ru@h-NSC and Ru@h-NC.

analysis in Fig. S9 (Supporting information), it can be concluded that Ru/RuS_2@h-NSC is consisted of only Ru, S, N and C elements, among which most of S is densely distributed around Ru, and a small fraction of S together with N is uniformly doped in carbon shells. Notably, the negligible P signal can be observed, indicating the absence of P element in Ru/RuS_2@h-NSC, despite abundant P source in the precursor.

To ascertain the role of P element in the formation of Ru/RuS_2 heterostructures in Ru/RuS_2@h-NSC, Ru(III)/COP-1@PS gained by the *in-situ* polymerization of TCA and cyanuric chloride (CC) without P was used as the precursor to generate Ru@h-NSC (Fig. S10a in Supporting information). The PXRD spectrum of Ru@h-NSC in Fig. 3a indicates that only Ru phase was generated. The further characterizations show that Ru@h-NSC also exhibits the hollow spherical structure with an average shell thickness of about 14 nm, where the Ru NPs of about 4.1 nm are homogeneously dispersed on the shell (Figs. S10b–f in Supporting information). In the HRTEM image in Fig. S10g (Supporting information), only the lattice fringes assigned to the hexagonal Ru phase are observed, further verifying the mere Ru phase with homogeneous dispersion on N/S doped carbon shell, as evidenced by the elemental mapping of Ru@h-NSC (Fig. S10h in Supporting information). Based on the structural contrast, it can be concluded that the P elements facilitate the formation of the Ru/RuS_2 heterostructures in Ru/RuS_2@h-NSC. It may due to the fact that the P evaporation could provide rich defects to immobilize Ru(III) species, leading to the easier bonding with the neighbouring S and yielding the Ru/RuS_2 heterostructures.

To further investigate the surface composition and chemical state of Ru/RuS_2@h-NSC, the X-ray photoelectron spectroscopy (XPS) analysis was performed. As shown in Fig. S11a (Supporting information), Ru, S, N and C elements can be detected in the survey spectrum of Ru/RuS_2@h-NSC. The high-resolution C 1s spectrum can be deconvolved into three peaks corresponding to C=C–C (284.8 eV), C–S (285.7 eV) and C–N (286.5 eV) (Fig. 3b). In addition, the peaks attributed to Ru^0 and Ru^{4+} can also be observed in the overlapped Ru 3d spectrum. The high-resolution Ru 3p spectrum of Ru/RuS_2@h-NSC in Fig. 3c further confirms the coexistence of Ru^0 and Ru^{4+} with the peaks at 462.4 and 465.98 eV, respectively. It is worth to note that the Ru^{4+} in Ru@h-NSC might be caused by the unavoidable air oxidation [39,40]. In the high-resolution S 2p spectrum in Fig. 3d, the characteristic peaks at 162.7 and 164.1 eV can be assigned to the S $2p_{3/2}$ and S $2p_{1/2}$ of S^{2-} in RuS_2. Except that, the peaks for polysulfides (S^0) at 164.1 and 165.3 eV and SO_4^{2-} at 168.6 eV are also observed, which may be interpreted as a consequence of surface oxidation during sample handling [41,42]. The high-resolution N 1s spectrum of Ru/RuS_2@h-NSC in Fig. S11b (Supporting information) can be convoluted into pyridine N (398.4 eV), pyrrolic N (399.6 eV), graphitic N (401.1 eV) and oxidized N (402.7 eV). The negligible P signal for Ru/RuS_2@h-NSC further certifies the absence of P element (Fig. S11c in Supporting information), in agreement with the TEM and EDX results. Notably, for the metallic Ru phase in Ru/RuS_2@h-NSC, a positive shift towards the higher binding energy (BE) can be observed compared to Ru@h-NSC without heterointerface. Simultaneously, a negative shift towards the lower BE for the S^{2-} in Ru/RuS_2@h-NSC also occurs as compared to RuS_2@NSC. This result is in accordance with the previous DFT prediction and indicates the redistributed charge density by the heterointerface construction, resulting in the electron transfer from metallic Ru phase to RuS_2 phase [26]. The relatively electron-deficient heterointerfacial Ru sites might be conducive to the adsorption of reaction intermediates.

The N_2 sorption isotherms were performed to probe the pore characteristics of Ru/RuS_2@h-NSC, Ru@h-NSC and Ru@h-NC without S doping (Figs. S12 and S13 in Supporting information). As it can be seen in Fig. 3e, an obvious hysteresis loop at higher pressure region is observed for Ru/RuS_2@h-NSC. Its corresponding pore size distributions in Fig. 3f and Fig. S14 (Supporting information) indicate the micro-mesoporous structure with an average mesopore size of about 4.25 nm, which can be attributed to the decomposition of the P/S/N-rich COP@PS during pyrolysis releasing bountiful P/S/N-containing gas and generating the mesoporous structure of carbon shell. Benefited from the rich mesopores in the N/S-doped hollow carbon microspheres of Ru/RuS_2@h-NSC, a specific BET surface area of 228.32 m^2/g can be provided, which is larger than that of Ru@h-NC (195.45 m^2/g) without S doping in carbon shell. The observed mesoporous structure of Ru/RuS_2@h-NSC is beneficial for accelerating the mass transport during the catalytic reactions.

Motivated by the highly exposed Ru/RuS_2 heterostructures homogeneously dispersed on the N/S-doped hollow carbon microspheres, the electrochemical HER performance of Ru/RuS_2@h-NSC was investigated, together with those of Ru@h-NSC, Ru@h-NC and commercial 20 wt% Pt/C for comparison. The Ru contents of Ru/RuS_2@h-NSC and compared samples are similar according to the ICP-AES results (Table S1 in Supporting information). Their LSV plots in 1.0 mol/L KOH electrolyte were firstly shown in Fig. 4a. As it can be seen, Ru/RuS_2@h-NSC exhibits the smallest onset potential and the most sharply increased current density toward HER among them. The higher activity of Ru/RuS_2@h-NSC is further confirmed by its small Tafel slopes (73.6 mV/dec), lower than those of Pt/C (76.2 mV/dec), Ru@h-NSC (91.2 mV/dec) and Ru@h-NC (115.2 mV/dec) (Fig. 4b). The overpotentials of Ru/RuS_2@h-NSC at 10 and 50 mA/cm^2 are only 26 and 87 mV, respectively, which are smaller than those of Pt/C (34 and 108 mV), Ru@h-NSC (96 and 179 mV) and Ru@h-NC (102 and 199 mV) (Fig. 4c). Surprisingly, when compared with the recently reported state-of-the-art HER electrocatalysts in alkaline solution, the small overpotential of Ru/RuS_2@h-NSC also manifests itself as a highly efficient electrocatalyst (Fig. 4d and Table S2 in Supporting information). Besides, to evaluate the electrocatalytic stability of Ru/RuS_2@h-NSC,

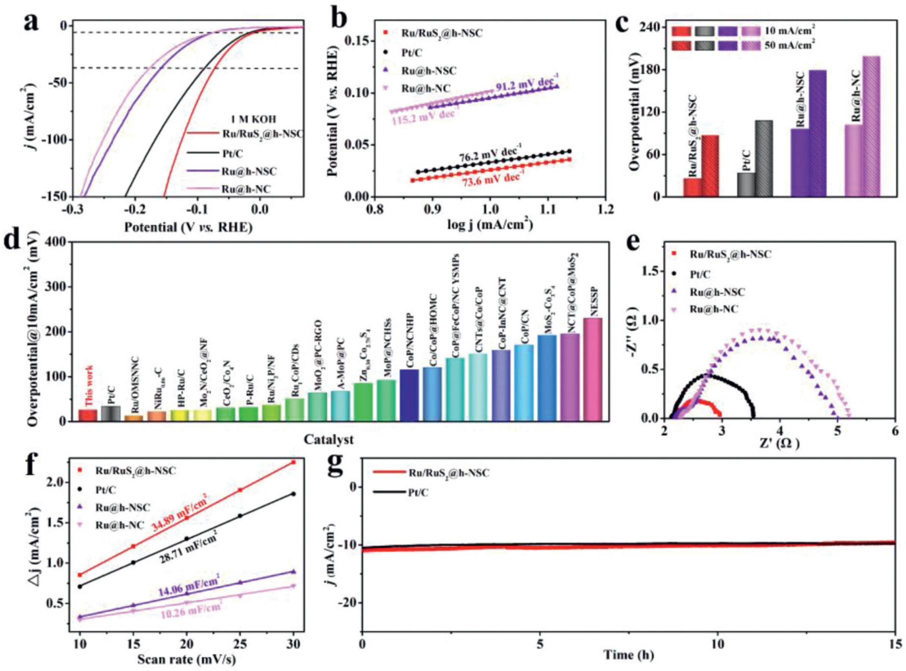

Fig. 4. (a) LSV plots, (b) Tafel plots, (c) overpotentials at 10 and 50 mA/cm^2 of Ru/RuS$_2$@h-NSC and comparative samples for HER in 1.0 mol/L KOH solution. (d) Comparison of the overpotentials achieved by recently reported representative HER catalysts in alkaline condition. (e) EIS and (f) C_{dl} plots of Ru/RuS$_2$@h-NSC and comparative samples. (g) Chronoamperometric measurement of Ru/RuS$_2$@h-NSC and commercial Pt/C.

the chronoamperometry measurements for 15 h was performed. As shown in Fig. 4g, the current density remains 93.9% of the initial value after the long-time electrolysis over Ru/RuS$_2$@h-NSC, which is comparable to Pt/C. Meantime, the crystalline structure and hollow sphere morphology remained unchanged after the test (Figs. S15 and S16 in Supporting information). These results indicate the excellent stability of Ru/RuS$_2$@h-NSC during the alkaline HER.

To explore the origin of the promoted activity of Ru/RuS$_2$@h-NSC, the EIS measurements reflecting the electron/proton transfer at the interface between catalyst and electrolyte were investigated. As shown in Fig. 4e and Table S3 (Supporting information), Ru/RuS$_2$@h-NSC has the smallest R_{ct} among these samples, which indicates its better conductivity and faster proton transfer between Ru/RuS$_2$@h-NSC and electrolyte, improving the catalytic kinetics. Furthermore, the ECSA that is correlated with the active site density was estimated by measuring the double-layer capacitances (C_{dl}) based on the CV at different scan rates. As displayed in Fig. 4f and Fig. S17 (Supporting information), Ru/RuS$_2$@h-NSC has a higher C_{dl} value of 34.89 mF/cm^2, compared to Pt/C (28.71 mF/cm^2), Ru@h-NSC (14.06 mF/cm^2) and Ru@h-NC (10.26 mF/cm^2). And the corresponding ECSA-normalized LSV plots in Fig. S18 (Supporting information) further verify the highest intrinsic activity of the active sites in Ru/RuS$_2$@h-NSC. To further identify the active sites of Ru/RuS$_2$@h-NSC towards alkaline HER, thiocyanate ions (SCN$^-$) as the metal-centered active site poisoner were introduced into the electrolyte. As shown in Fig. 5a, upon the addition of SCN$^-$ ions, an obvious decrease in current density can be observed for Ru/RuS$_2$@h-NSC, revealing the active site nature of the Ru NPs. In addition, by changing the dosage of Ru source during the preparation of Ru/RuS$_2$@h-NSC, the component of the Ru/RuS$_2$ heterostructures can be controlled. As displayed in Figs. S19 and S20 (Supporting information), the preferential formation of metallic Ru over RuS$_2$ was found with the dosages lower than 0.2 mmol, whereas the reverse appeared with the higher dosages. Meantime, the higher catalytic activity is only observed over Ru/RuS$_2$@h-NSC with the obvious presence of both metallic Ru and RuS$_2$ phases (Fig. 5b and Fig. S21 in Supporting information), evidencing the useful heterointerface between them for improving the HER activity. Furthermore, as displayed in Fig. S5, under the calcination temperature below 800 °C, the better crystallinity of both small Ru and RuS$_2$ NPs was observed with elevating the calcination temperature, yielding the more interfacial Ru atoms in Ru/RuS$_2$ heterostructure and thereby the higher catalytic activity of Ru/RuS$_2$@h-NSC (Fig. 5c and Fig. S22 in Supporting information). It is noted that further increasing the calcination temperature to 900 °C led to the agglomeration of the NPs and the collapse of spherical structure, dramatically decreasing the activity.

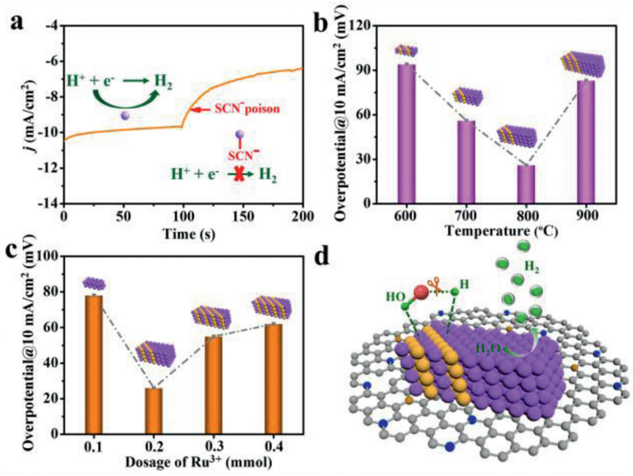

Fig. 5. (a) Current-time (*i-t*) curve of Ru/RuS$_2$@h-NSC upon the addition of SCN$^-$ ions in 1.0 mol/L KOH solution. Overpotentials at 10 mA/cm^2 of Ru/RuS$_2$@h-NSC prepared (b) with different dosages of RuCl$_3$ and (c) at different temperatures. (d) The proposed HER mechanism over Ru/RuS$_2$@h-NSC.

Generally during the alkaline HER process, the water dissociation and hydrogen absorption occurs on different active sites. The HER kinetics can be optimized by regulating the binding energy of hydrogen and hydroxyl species on dual active sites. Based on the

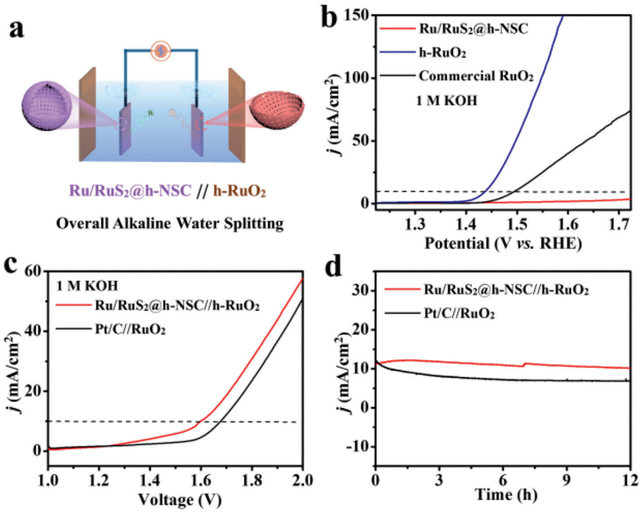

Fig. 6. (a) Schematic representation for the overall alkaline water splitting. (b) LSV plots of h-RuO_2 and compared samples for OER. (c) LSV plots of the Ru/RuS_2@h-NSC||h-RuO_2 cell and Pt/C||commercial RuO_2 cell for water splitting. (d) Chronopotentiometric measurement over the Ru/RuS_2@h-NSC||h-RuO_2 cell.

measured Tafel slope value of 73.6 mV/dec, the alkaline HER reaction over Ru/RuS_2@h-NSC follows the Volmer–Heyrovsky step including the water dissociation to surface-bonded H* and OH*, the desorption of OH* rate-determining the overall reaction and then the desorption of H* to gaseous H_2 [43]. On the Ru/RuS_2 heterointerface, OH* could preferentially attaches to the RuS_2 sites due to the electrostatic affinity to the locally positively charged Ru^{4+} species, while the H* absorption tends to happen on the relatively electron-deficient Ru atoms of interfacial Ru NPs [44]. The synergistic absorption of the intermediates contributes to lowering the energy barrier for water dissociation and facilitating the H* absorption, thus accelerating the overall alkaline HER kinetic as illustrated in Fig. 5d. In addition, the spherical nanostructure with abundant mesopores enables the active sites on both outer and inner shells to be more accessible. The hollow cavity as an electrolyte reservoir can also make the electrolyte easy to penetrate into the micropores and mesopores of Ru/RuS_2@h-NSC, greatly accelerating the mass transport. Based on the above results, it can be concluded that the synergistic effect between heterointerfacial Ru/RuS_2, the high accessibility of the active sites and the efficient mass transport in the hollow structure jointly contribute to the extraordinary HER performance of Ru/RuS_2@h-NSC. To validate the synergistic effect between heterointerfacial Ru/RuS_2 in accelerating the water dissociation step of HER, the HER performance of Ru/RuS_2@h-NSC was also investigated in 1.0 mol/L PBS electrolyte. As show in Fig. S23 (Supporting information), the overpotential of Ru/RuS_2@h-NSC is 130 mV at 10 mA/cm^2 in 1.0 mol/L PBS solution, which is smaller than those of Pt/C (148 mV) and other compared samples (over 300 mV), similar to that in alkaline condition. While for the acidic HER without the water dissociation step, the activity of Ru/RuS_2@h-NSC is inferior to Pt/C in 0.5 mol/L H_2SO_4 (Fig. S24 in Supporting information). Such phenomenon further verifies the advantage of the heterostructure for accelerating the water dissociation during the HER.

To examine practical feasibility of Ru/RuS_2@h-NSC for H_2 production, the overall alkaline water splitting in a two-electrode system was constructed by using Ru/RuS_2@h-NSC as the cathode (Fig. 6a). Taking advantage of the hollow mesoporous spherical structure with homogenous distribution of Ru/RuS_2, Ru/RuS_2@h-NSC was easily converted into the hollow RuO_2 nanobowls by pyrolysis at 350 °C in air, denoted as h-RuO_2 for simplicity. The characterizations of h-RuO_2 in Figs. S25 and S26 (Supporting information) verify the formation of hollow bowl-like RuO_2. Furthermore, the higher activity of h-RuO_2 than that of commercial RuO_2 towards the oxygen evolution reaction (OER) can be observed in Fig. 6b, which motivates the employment of h-RuO_2 as the anode for the overall water splitting. As shown in Fig. 6c, the assembled Ru/RuS_2@h-NSC||h-RuO_2 cell only needs a voltage of 1.6 V@10 mA/cm^2 to drive the overall water splitting, lower than that of the commercial Pt/C||RuO_2 cell (1.7 V@10 mA/cm^2). In addition, the long-term electrolysis at 10 mA/cm^2 in Fig. 6d also manifests the excellent stability of the Ru/RuS_2@h-NSC||h-RuO_2 cell.

In conclusion, the Ru/RuS_2@h-NSC with highly exposed Ru/RuS_2 heterostructures evenly dispersed on the N/S-doped hollow carbon microspheres was synthesized by using the P/S/N-rich COP as the trapping agent for Ru(III) species. Benefited from the synergistic effect between heterointerfacial Ru/RuS_2, the high accessibility of the active sites on the inner/outer surface and the efficient mass transport in the mesoporous hollow structure, Ru/RuS_2@h-NSC exhibits the preeminent electrocatalytic performance with an overpotential of 26 mV@10 mA/cm^2 and a Tafel slope of 73.6 mV/dec for alkaline HER, outperforming most of the state-of-the-art catalysts. Furthermore, by assembling Ru/RuS_2@h-NSC and derived h-RuO_2 in the overall alkaline water splitting electrolyzer, the required cell voltage of Ru/RuS_2@h-NSC||h-RuO_2 is 100 mV lower than that of the commercial Pt/C||RuO_2 cell. Our study may allow us to guide the preparation of advanced nanomaterials with controllable morphologies and heterostructures for promising application in electrocatalysis.

Declaration of competing interest

The authors declare that they have no known competing financial interests or personal relationships that could have appeared to influence the work reported in this paper.

Acknowledgments

This work was financially supported by the National Key R&D Program of China (No. 2021YFA1500402), the National Natural Science Foundation of China (NSFC, Nos. 21901246, 22105203 and 22175174), and the Natural Science Foundation of Fujian Province (Nos. 2020J01116 and 2021J06033).

Supplementary materials

Supplementary material associated with this article can be found, in the online version, at doi:10.1016/j.cclet.2022.107788.

References

[1] F. Liu, C. Shi, X. Guo, et al., Adv. Sci. 9 (2022) e2200307.
[2] X.X. Zou, Y. Zhang, Chem. Soc. Rev. 44 (2015) 5148–5180.
[3] J. Greeley, T.F. Jaramillo, J. Bonde, I.B. Chorkendorff, J.K. Norskov, Nat. Mater. 5 (2006) 909–913.
[4] V.R. Stamenkovic, D. Strmcnik, P.P. Lopes, N.M. Markovic, Nat. Mater. 16 (2017) 57–69.
[5] B. You, Y.J. Sun, Acc. Chem. Res. 51 (2018) 1571–1580.
[6] K. Zeng, D.K. Zhang, Energy Combust. Sci. 36 (2010) 307–326.
[7] X.P. Yin, S.W. Luo, S.F. Tang, et al., Chin. J. Catal. 42 (2021) 1379–1386.
[8] T. Wang, X. Cao, L. Jiao, eScience 1 (2021) 69–74.
[9] C.B. Hong, X. Li, W.B. Wei, X.T. Wu, Q.L. Zhu, Appl. Catal. B 294 (2021) 120230.
[10] Y. Li, L.A. Zhang, Y. Qin, et al., ACS Catal. 8 (2018) 5714–5720.
[11] Y.L. Wu, X. Li, Y.S. Wei, et al., Adv. Mater. 33 (2021) e2006965.
[12] Y. Deng, L. Yang, Y. Wang, et al., Chin. Chem. Lett. 32 (2021) 511–515.
[13] M. Li, H. Wang, W. Zhu, et al., Adv. Sci. 7 (2020) 1901833.
[14] Y. Liu, X. Li, Q. Zhang, et al., Angew. Chem. Int. Ed. 59 (2020) 1718–1726.
[15] J. Mao, C.T. He, J. Pei, et al., Nat. Commun. 9 (2018) 4958.
[16] Y. Xu, S. Yin, C. Li, et al., J. Mater. Chem. A 6 (2018) 1376–1381.
[17] Y.L. Wu, N. Xie, X. Li, et al., Chin. J. Struct. Chem. 40 (2021) 1346–1356.
[18] B. Lu, L. Guo, F. Wu, et al., Nat. Commun. 10 (2019) 631.
[19] H. Tao, C. Choi, L.X. Ding, Z. Sun, et al., Chem 5 (2019) 204–214.
[20] H. Zhang, W. Zhou, X.F. Lu, T. Chen, X.W. Lou, Adv. Energy Mater. 10 (2020) 2000882.

[21] X. Chen, J. Zheng, X. Zhong, et al., Catal. Sci. Technol. 7 (2017) 4964–4970.
[22] P. Jiang, Y. Yang, R. Shi, et al., J. Mater. Chem. A 5 (2017) 5475–5485.
[23] S.H. Ye, F.Y. Luo, T.T. Xu, et al., Nano Energy 68 (2020) 7.
[24] S.Z. Dong, Y.S. Li, Z.L. Zhao, et al., ChemistrySelect 7 (2022) e202104041.
[25] G.Q. Zhao, K. Rui, S.X. Dou, W.P. Sun, Adv. Funct. Mater. 28 (2018) 1803291.
[26] J.W. Zhu, Y. Guo, F. Liu, et al., Angew. Chem. Int. Ed. 60 (2021) 12328–12334.
[27] Q. Fu, X. Wang, J. Han, J. Zhong, et al., Angew. Chem. Int. Ed. 60 (2021) 259–267.
[28] C.T. Dinh, A. Jain, F.P.G. de Arquer, et al., Nat. Energy 4 (2018) 107–114.
[29] K.L. Zhou, Z. Wang, C.B. Han, et al., Nat. Commun. 12 (2021) 3783.
[30] M. Zhang, J. Chen, H. Li, et al., Nano Energy 61 (2019) 576–583.
[31] X. Cui, L. Gao, R. Ma, et al., J. Mater. Chem. A 9 (2021) 20985–21004.
[32] L. Sun, M. Lu, Z. Yang, et al., Angew. Chem. Int. Ed. 61 (2022) e202204326.
[33] Z. Xiang, Y. Xue, D. Cao, et al., Angew. Chem. Int. Ed. 53 (2014) 2433–2437.
[34] J. Zhang, Y. Wang, H. Wang, et al., Chin. Chem. Lett. 33 (2022) 2065–2068.
[35] J. Fu, X. Huang, Y. Huang, et al., J. Phys. Chem. C 112 (2008) 16840–16844.
[36] D. Ko, J.S. Lee, H.A. Patel, et al., J. Hazard. Mater. 332 (2017) 140–148.
[37] D.D. Ma, C. Cao, X. Li, et al., Electrochim. Acta 321 (2019) 134679.
[38] X. Jie, W. Li, D. Slocombe, Y. Gao, et al., Nat. Catal. 3 (2020) 902–912.
[39] L. Su, Y. Zhao, Y. Jin, et al., Adv. Funct. Mater. (2022) 2113047.
[40] Y. Qin, W. Zhang, F. Wang, et al., Angew. Chem. Int. Ed. 61 (2022) e202200899.
[41] Y. Huang, L.W. Jiang, H. Liu, J.J. Wang, Chem. Eng. J. 441 (2022) 136121.
[42] A. Matamoros-Veloza, O. Cespedes, B.R.G. Johnson, et al., Nat. Commun. 9 (2018) 3125.
[43] I.T. McCrum, M.T.M. Koper, Nat. Energy 5 (2020) 891–899.
[44] M. Gong, W. Zhou, M.C. Tsai, et al., Nat. Commun. 5 (2014) 4695.